

# Evolution of iron-containing defects during processing of Si solar cells

Teimuraz Mchedlidze,<sup>1,a)</sup> Christian Möller,<sup>2</sup> Kevin Lauer,<sup>2</sup> and Jörg Weber<sup>1</sup>

<sup>1</sup>Technische Universität Dresden, 01062 Dresden, Germany

<sup>2</sup>CiS Forschungsinstitut für Mikrosensorik und Photovoltaik GmbH, Konrad-Zuse-Str. 14, 99099 Erfurt, Germany

(Received 25 July 2014; accepted 13 December 2014; published online 23 December 2014)

The formation of iron-containing defects was studied during the fabrication process of a Si solar cell. Three Cz-Si crystals with different iron content in the feedstock were grown for the study. Iron-containing defects in and near-to the  $n^+p$ -junction volume (NJV) of the cells are formed directly after phosphorus diffusion due to an inflow of iron atoms from the dissolving iron-silicide precipitates. These NJV-defects strongly affect the dark saturation current of the junctions. Partial dissolution or gettering of the NJV-defects during formation of the antireflection coating is accompanied by an increase in defect concentrations in the bulk of the cell. Further deterioration of bulk carrier lifetime during the formation of electrical contacts is related to the partial dissolution of remaining iron-silicide precipitates during the firing process. A general description of the defect evolution in iron-contaminated wafers during solar cell processing is presented and possible strategies for reducing the influence of iron-containing defects are proposed. © 2014 AIP Publishing LLC. [<http://dx.doi.org/10.1063/1.4905027>]

## I. INTRODUCTION

The costs for Si solar cells could be substantially reduced if Cz-crystals were grown from feedstock with inferior purity.<sup>1</sup> The iron specification of the feedstock is most critical due to the strong detrimental effect of Fe on the solar cell performance (see Refs. 2–4 and references therein), the high prevalence of Fe in the Si feedstock<sup>1</sup> and the difficulties in passivating or gettering of iron-related defects.<sup>5</sup> A recent study<sup>6</sup> verifies that the melt is the source of the Fe contamination in the crystal and that the Fe atoms are nearly equally distributed over the wafers. Various Fe-containing defects, complexes, and precipitates were detected in these wafers (see, e.g., Refs. 5, 7–11, and references therein), which transform under intense light illumination and/or treatments at moderate temperatures.<sup>5</sup>

The solubility limit determines the concentration  $\{Fe_{diss}\}$  of iron atoms that are dissolved in the silicon lattice at a certain temperature.<sup>5</sup> If the total iron concentration  $\{Fe_{tot}\}$  is larger than  $\{Fe_{diss}\}$ , segregation of iron-silicide precipitates and various iron-containing complexes is expected. After the conventional slow after-growth cooling of the Si crystal,  $\{Fe_{diss}\}$  presents only a small fraction of  $\{Fe_{tot}\}$ . In p-type boron doped Si, used for base material in photovoltaics, the dissolved iron atoms exists at room temperature as interstitial Fe ( $Fe_i$ ) and/or as FeB pairs.<sup>5</sup> The reversible reaction  $FeB \leftrightarrow Fe_i + B_S$  occurs easily under illumination and/or moderate temperature treatments. The concentrations  $\{Fe_i\}$  and  $\{FeB\}$  are reliably and directly measured by deep level transient spectroscopy (DLTS).<sup>5</sup> The total Fe contamination  $\{Fe_{tot}\}$ , including the iron

content in iron-silicide precipitates could be determined by SIMS or chemical analysis but with low sensitivity. Recently, we reported on a simple method which allows the measurement of  $\{Fe_{tot}\}$  directly by DLTS.<sup>6</sup> The method involves a very fast quench of the iron-contaminated sample from a temperature where all iron atoms are dissolved in the lattice (high temperature annealing and quenching—HTAQ). The fast quenching prevents iron precipitation and preserves iron as  $Fe_i$  and/or FeB, which can be detected by DLTS. The sum  $\{Fe_i\}$  and  $\{FeB\}$  in the HTAQ treated sample gives  $\{Fe_{tot}\}$ .

The fabrication of silicon solar cells involves several processing steps, e.g., dopant diffusion, surface coatings, electrical contact formation, etc., which all affect the iron-containing defects in the wafers. A better understanding of the behaviour of iron during solar cell fabrication could suggest modifications of the processing steps and could improve solar cell efficiencies by reducing the fabrication costs at the same time. The influence of an iron contamination on the efficiency of a solar cell was previously studied and a critical iron concentration was suggested, which could be tolerated by the specific solar cell fabrication process.<sup>12–15</sup> However, the influence of the different processing steps on the formation of the specific iron-defects was not clarified. A proper knowledge of the influence of certain processing steps on the defects could lead to modifications which would allow an increase in the critical iron concentration in the feedstock.<sup>15</sup>

Recently, we reported on changes of the bulk carrier lifetime after different solar cell fabrication processes using Cz-Si wafers containing iron.<sup>16</sup> In the same material, carrier traps in/and near-to junction volume (NJV defects) were detected by DLTS after formation of  $n^+p$ -junctions.<sup>12,17</sup>

In the present paper, we study the influence of the NJV traps on the diode characteristics of solar cells and clarify

<sup>a)</sup> Author to whom correspondence should be addressed. Electronic mail: teimuraz.mchedlidze@physik.tu-dresden.de Phone: +49 351463 37227. Fax: +49 351 463 37060

the interaction of bulk and NJV defects in processed Cz-Si solar cell wafers. The results will be compared to those reported in previous investigations.<sup>12,16,17</sup>

## II. SAMPLES AND EXPERIMENTAL

Three Si crystals were specially grown for the study in the standard Cz-process and each feedstock used for their growth was contaminated intentionally with iron to a different level. These crystals were labeled *A*, *B*, and *C* in our previous work.<sup>16</sup> The crystals were doped with boron to obtain a resistivity in the range of 3–6 Ωcm. Standard sized, 150 μm thick and 156×156 mm<sup>2</sup> squared Si wafers were cut from the lower quarter of the Cz-Si ingots. The {Fe<sub>tot</sub>} concentrations in the as-grown samples were determined by DLTS after the HTAQ process.<sup>6</sup> Results are presented in Table I. A commercial Cz-Si solar cell wafer was used as reference sample (*Ref*) which showed a total iron content below the background contamination level of our HTAQ procedure ( $<1 \times 10^{12} \text{ cm}^{-3}$ ).

The A-C wafers were subjected to the processing steps of a standard, consecutive solar cell fabrication process.<sup>16,18</sup> The steps can be grouped in four stages: (i) The cleaning stage (*C*) with the saw damage removal by KOH and RCA cleaning. (ii) The phosphorus diffusion stage (*P*) was done in a walking string inline furnace. The phosphorus dopant was deposited by spray coating of phosphoric acid solution. The phosphorus in-diffusion thermal treatment was followed by phosphor-silicate glass removal and cleaning. (iii) The anti-reflection coating (*R*) stage consists of a Si<sub>3</sub>N<sub>4</sub> layer deposition in a PECVD reactor followed by an appropriate temperature treatment. (iv) At the last stage (*E*), the electrical contacts were formed by screen printing of Ag (front bus bars) and Al (back contact) pastes, solvent evaporation, and sintering. As a variation or simulation (*S*) of the antireflection coating stage, the similar to the *R* stage temperature treatment was performed on several cells without pre-deposition of nitride layers. All processes were performed at CiS (Erfurt, Germany). Further details and parameters, i.e., temperatures, durations, etc., of the solar cell process are given in Ref. 16. The samples will be labeled as follows: after the name of the crystal (*A*, *B*, *C*), an additional letter will specify the last processing stage of the sample (*C*, *P*, *R*, *E*, or *S*, see Table I).

Measurements of the current-voltage (*IV*) characteristics of the solar cell after stage *E* were performed using mesa-diodes with an area of ~1–3 mm<sup>2</sup>. The preparation of the mesa-diodes directly from the solar cells was described in Ref. 17. In addition, we evaluated larger diode areas for *IV*-measurements by cutting pieces (chips) with an area of ~4 cm<sup>2</sup> from the finished solar cell.

Room temperature current-voltage measurements were performed with a PC-controlled Keithley 2601 SourceMeter. The samples were placed in a light-tight, electrically shielded box during the measurements. Efficiency measurements of the finished solar cells showed a large scatter even for sister wafers of the same crystal. We attribute these variations to the scatter in the optical properties of the cells, since texturization of the wafer surfaces was not performed.

Therefore, we were unable to use the efficiency for characterization of our cells.

Details of DLTS and lifetime measurements on the cells were presented previously.<sup>12,16</sup> For the cleaned wafer (after the stage *C*), the Schottky contact was evaporated directly on the front surface of the wafer for DLTS measurements and ohmic contacts were formed by rubbing-in InGa eutectic solution to the back surface. Near-to-junction volume of the cells (after stages *P*, *R*, *E* and *S*) was characterized using DLTS signals from mesa-diodes. The bulk defects were characterized by measuring DLTS and/or carrier lifetime on locations adjacent to mesa-diode positions. The n<sup>+</sup>p-junction structures were completely eliminated by etching away ~50 μm from the surface of the cells for these measurements. For DLTS measurements of the samples with removed cell structures, the Schottky diodes were fabricated as was described above.

## III. RESULTS AND DISCUSSION

### A. Current-voltage measurements

Determination of the dark saturation current density ( $J_D$ ) due to recombination in the space-charge region (SCR) of a solar cell is used to estimate the recombination lifetime of charge carriers ( $\tau_D$ , see, e.g., Ref. 19)

$$\tau_D = \frac{qn_i W_D}{J_D}, \quad (1)$$

here  $q$  is electron charge,  $n_i$  is intrinsic carrier density,  $W_D$  is the voltage dependent SCR width. Usually,  $J_D$  is determined from measurements of the *IV*-curve from a whole solar cell in the dark (see, e.g., Ref. 20). However, correct determination of  $J_D$  implies a homogeneous distribution of current density across the whole area of the junction. That is not the case for a wafer with a solar cell structure where during *IV*-measurements the carriers are injected mainly from the bus bars due to lower emitter conductance, resulting in highly inhomogeneous current distributions. Therefore, the *IV*-curve of a “whole-cell” actually presents a superposition with largely diverse current-density values. Besides that the data extraction from a whole-cell measurement is complicated by large series resistances and high leakage conductance values  $G_L$ .

Current-voltage measurements should therefore be performed on small area mesa-diode-type structures etched on the top of a solar cell. Examples of current density-voltage (*JV*) curves for the *Ref* sample are presented in Fig. 1(a). Curve (1) is from a ~3.5 cm<sup>2</sup> area cleaved piece (chip) of the solar cell and (2) is from a ~1 mm<sup>2</sup> area mesa-diode fabricated on the surface of the cell. The results from the mesa-diode show much better correspondence to a near-ideal diode (see, e.g., Ref. 21). Estimations of shunt resistance values from the reverse characteristics of the samples suggest ~50 kΩ/cm<sup>2</sup> for the chip of the cell and >2 MΩ/cm<sup>2</sup> for the mesa-diode. Example *JV* curves for mesa-diodes of A-C and *Ref* samples are presented in Fig. 1(b).

Different methods to extract diode parameters from *IV*-curves of solar cells were recently compared<sup>20</sup> and showed similar results. For our analysis of the *IV*-data, we used the

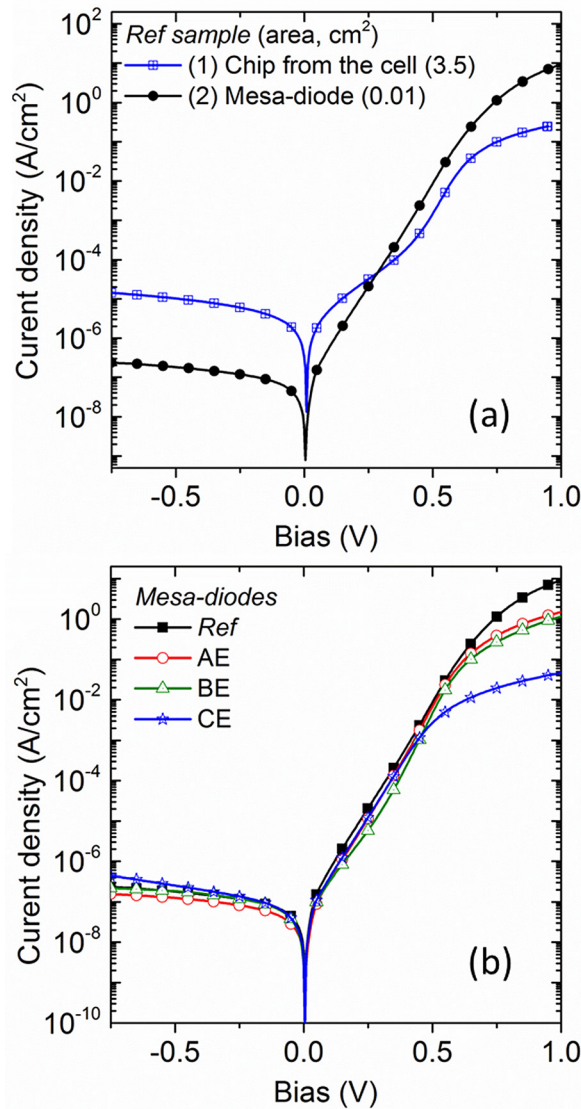


FIG. 1. (a)  $JV$ -curves of different diodes from the *Ref* sample. For details, see text. (b)  $JV$ -curves from mesa-diodes prepared from different crystals. Measuring conditions: no illumination, voltage step 5 mV,  $T_{\text{meas}} = 295$  K.

so-called “derivative method”<sup>22</sup> The method allows the determination of the ideality factor ( $n$ ), the dark saturation current ( $J_D$ ), shunt ( $R_{\text{SH}}$ ), and series ( $R_{\text{SER}}$ ) resistances from the forward biased  $JV$  curve by plotting the bias dependent differential slope curve  $\alpha(V) = [d(\ln I)]/[d(\ln V)]$ . To obtain reliable data from 12 to 18, mesa-diodes from each sample were tested.

The ideality factors for the mesa-diodes were in the range from 1.28 (*Ref* sample) to 1.42 (AE sample), while they were much larger ( $1.58 \div 1.76$ ) when estimated from the chips of the relevant cells. High values for  $R_{\text{SH}} \geq 1 \text{ M}\Omega/\text{cm}^2$  substantially simplified the determination of the parameters for the mesa-diodes.<sup>22</sup> The values of  $R_{\text{SER}}$  were in the range of  $0.1 \div 0.4 \text{ }\Omega/\text{cm}^2$  for the mesa-diodes and by an order of magnitude larger for the chips. The values for dark saturation current densities,  $J_D$  are presented in Fig. 2, in relation to  $\{\text{Fe}_{\text{tot}}\}$  in the crystals (see Table I). The values obtained for the chips are also given for comparison.

The  $J_D$  values of the mesa-diodes show a clear correlation with  $\{\text{Fe}_{\text{tot}}\}$  of the original wafers (see Fig. 2). The mesa diode of the *Ref* sample gave the lowest current density. Evaluation of the data from the measurements of the samples in the form of the chips showed much higher  $J_D$  values. We suppose that the extraction procedure of the diode parameters for the chips was largely affected by the current distributions and by large  $G_L$  values. Therefore, the data for the chips do not reflect correctly the material properties and cannot be used for proper characterization of the material properties. Only the results for the mesa-diodes will be analyzed in the remaining part of the paper.

## B. Correlation of NJV trap densities with $J_D$

From  $J_D$ , the carrier lifetime in the space charge region can be estimated according to Eq. (1). We used the  $W_D$  value at zero bias for the estimations. The dominant traps detected in all diodes in the NJV were TM1.<sup>12</sup> As it was reported previously,<sup>12,17</sup> the TM1 trap distribution is inhomogeneous, i.e., TM1 density steeply decreases with the distance from the junction. The TM1 trap density, integrated by depth was proposed in Ref. 12 as a measure for the trap quantity in a sample. These values will be labelled  $\{\text{NJV}\}$  below. The correlation of the carrier lifetime with the  $\{\text{NJV}\}$  is presented in Fig. 3.

The strong decrease in lifetime with increasing  $\{\text{NJV}\}$  values indicates that the TM1 traps are the dominant lifetime killers in the NJV. A connection of the lifetime to the capture cross-section of the TM1 traps, detected by DLTS, cannot be derived due to inhomogeneous distribution of the traps.

## C. Interaction and interrelation between NJV traps and defects in the bulk of the cells

The measurements performed on the bulk material of the processed solar cells supplied information for bulk carrier lifetime,  $\tau_{\text{Eff}}$  and  $\{\text{Fe}_{\text{diss}}\}$  after various fabrication

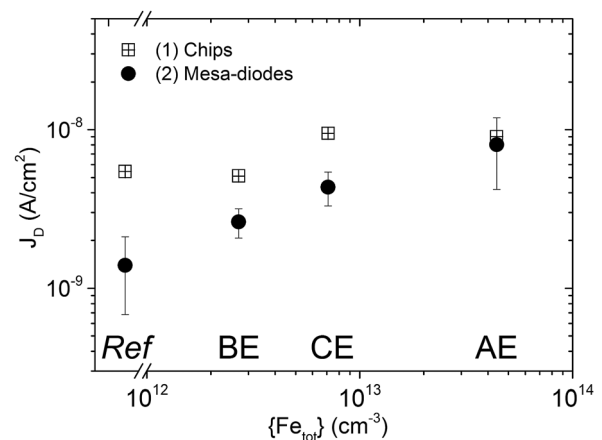


FIG. 2. Dark saturation current density ( $J_D$ ) of mesa diodes from the finished solar cells compared to the total iron content  $\{\text{Fe}_{\text{tot}}\}$  in the crystals *Ref.*, *A*, *B*, and *C*. Results from 12–18 mesa-diodes structures were averaged for each sample. For comparison,  $J_D$  values for the chips are also given with different symbols.



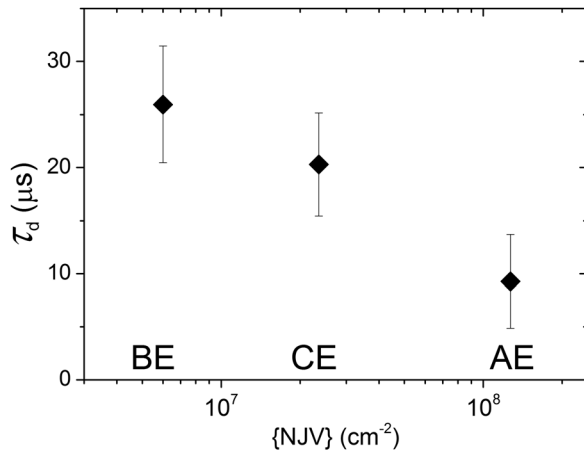


FIG. 3. Correlation between  $\tau_D$  and depth-integrated trap densities in near-to junction volume of the AE-CE samples {NJV}.

processes.<sup>16</sup> A reciprocal of  $\tau_{\text{Eff}}$  is proportional to overall trap concentration in the bulk<sup>19</sup> and therefore  $\{N_t\} = 1/\tau_{\text{Eff}}$  can be used as a value reflecting relative quantity of the bulk defects. We would like to compare behaviors of {NJV}, {Fe<sub>diss</sub>} and  $\{N_t\}$  after various solar cell fabrication processes in samples with various {Fe<sub>tot</sub>}.

A comparison of {Fe<sub>tot</sub>} with {Fe<sub>diss</sub>} confirms that most of the iron in the as-grown crystals is contained in iron-silicide precipitates.<sup>23</sup> Indeed, a ratio of the dissolved iron to the total concentration for A and B crystals is around 0.1% and it is ~7.7% for crystal C. The origin of the relatively large fraction of non-precipitated iron in the C crystal is not clear and may be related to some specific (but unknown to us) thermal history of this crystal.

Normalized values of {NJV}, {Fe<sub>diss</sub>}, and  $\{N_t\}$  for the C crystal after the processing stages are presented in Fig. 4. The plot is divided into two parts. The left part shows variations in the concentrations for the complete fabrication process: CC→CP→CR→CE, while the right part illustrates the changes in the case of CP→CS sequence. The results indeed suggest that the processing stages lead to different changes in the measured defect concentrations. For example, for the CP→CR step {NJV} falls by a factor of ten, {Fe<sub>diss</sub>} is reduced by a factor of two, while  $\{N_t\}$  slightly increases. However, in some cases, similar changes occur, e.g., in the case of CR→CE or CP→CS steps.

As a measure of the changes, the ratio of concentrations after the processing stage to the concentrations before the processing stage can be used. We will label the ratio by the fraction of the sample labels (see Table I) followed by the specific defect type in parenthesis. For example, BS/BP{NJV} will denote the ratio of {NJV} after processing stage S to {NJV} after stage P in the crystal B. Figure 5 presents examples of such ratios for processed samples from the A-C crystals. On the horizontal axis, the processing stage ratios are specified.

A large decrease in {Fe<sub>diss</sub>} was detected after phosphorus diffusion in A and C crystals: AP/AC{Fe<sub>diss</sub>}, CP/CC{Fe<sub>diss</sub>} ≪ 1. Contrary, despite the expected gettering effect during phosphorus diffusion, {Fe<sub>diss</sub>} nearly tripled for

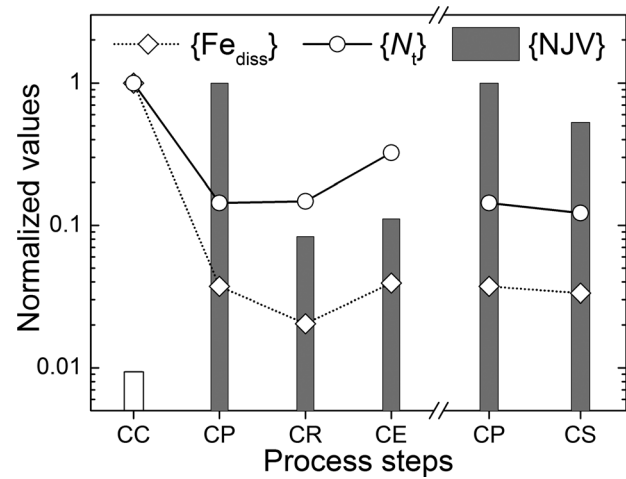


FIG. 4. Normalized values of {Fe<sub>diss</sub>},  $\{N_t\}$ , and {NJV} after different processing stages of wafers from crystal C. No NJV defects were detected before phosphorus diffusion; therefore, the detection limit for TM1 traps is shown in the case of the CC process. Points are connected to guide the eye.

the crystal B: BP/BC{Fe<sub>diss</sub>} > 3. A possible explanation is as follows. Due to a higher {Fe<sub>tot</sub>} in the A and C crystals, iron-silicide precipitates were larger in size and in density than in the B crystal. The phosphorus diffusion process caused only a partial dissolution of the iron-silicide precipitates in A and C and those precipitates that survived, served as gettering centers during the relatively fast cooling after the process. For B, the phosphorus diffusion process caused nearly a complete dissolution of the iron-silicide precipitates and a substantial number of iron atoms were quenched in at interstitial sites due to absence of precipitation sites. Note also that the level of {Fe<sub>diss</sub>} after the P process was minimal in the A crystal,<sup>16</sup> where {Fe<sub>tot</sub>} was the largest.

Influence of the R process on {Fe<sub>diss</sub>} appears also dependent on the crystals: BR/BP{Fe<sub>diss</sub>} < CR/CP{Fe<sub>diss</sub>} < 1 < AR/AP{Fe<sub>diss</sub>}. The changes are inverse to those detected for {NJV}: BR/BP{NJV} > CR/CP{NJV} > AR/AP{NJV}. We suppose that a flow of iron atoms from dissolving NJV traps into the crystal could explain the changes of {Fe<sub>diss</sub>}

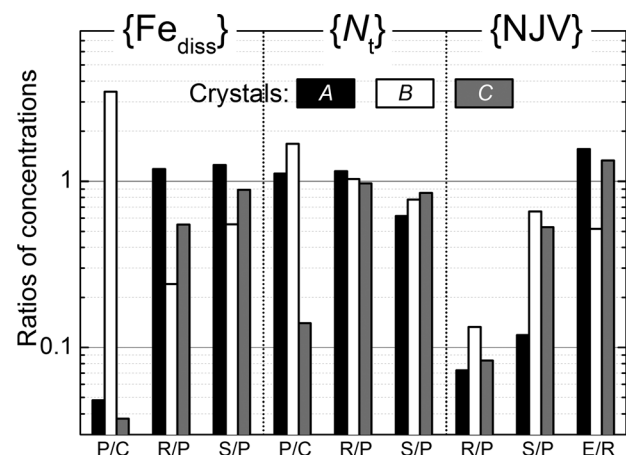


FIG. 5. Ratios of {Fe<sub>diss</sub>},  $\{N_t\}$ , and {NJV} values after various processing stages to those before for the three crystals A-C.

TABLE I. Total iron concentration  $\{\text{Fe}_{\text{tot}}\}$  in the *A*, *B*, and *C* crystals measured after HTAQ treatments; labeling of the samples subjected to various treatments and/or fabrication processes.

Crystal {Fe <sub>tot</sub> } ( $\times 10^{12} \text{ cm}^{-3}$ )	<i>A</i> 44 ± 6	<i>B</i> 2.7 ± 0.4	<i>C</i> 7.1 ± 0.4
Process	Sample labels <sup>a</sup>		
(C): <i>C</i>	AC	BC	CC
(P): <i>C</i> + <i>P</i>	AP	BP	CP
(R): <i>C</i> + <i>P</i> + <i>R</i>	AR	BR	CR
(S): <i>C</i> + <i>P</i> + <i>S</i>	AS	BS	CS
(E): <i>C</i> + <i>P</i> + <i>R</i> + <i>E</i>	AE	BE	CE

<sup>a</sup>“#” in the label will be used as a wildcard.

during the *R* process. Interestingly, despite an substantial influence of the *R* process on  $\{\text{Fe}_{\text{diss}}\}$ , the bulk defect concentration remains almost unchanged for all crystals:  $\#R/\#P\{N_t\} \approx 1$  (here and later “#” is used as a wildcard for the crystal labels). This effect could again be attributed to the inflow of traps from NJV to the bulk.

Dissolution and/or passivation of NJV traps is strongly enhanced in the presence of a nitride layer:  $\#R/\#P\{NJV\} < \#S/\#P\{NJV\}$  (see Fig. 5). At the same time,  $\#R/\#P\{N_t\} > \#S/\#P\{N_t\}$  suggests that annealing without the  $\text{Si}_3\text{N}_4$  layer suppresses better the recombination centers in the bulk. This could also be attributed to a reduced inflow of traps from the NJV without a  $\text{Si}_3\text{N}_4$  layer. In addition, the presence of the nitride film differently affects the total density of bulk defects and the dissolved iron concentration in the bulk:  $\#R/\#P\{\text{Fe}_{\text{diss}}\} < \#S/\#P\{\text{Fe}_{\text{diss}}\}$ , while  $\#R/\#P\{N_t\} > \#S/\#P\{N_t\}$ .

The positive effect of the remaining amount of iron-silicide precipitates after phosphorus gettering, i.e.,  $\text{AP}/\text{AC}\{\text{Fe}_{\text{diss}}\}$ ,  $\text{CP}/\text{CC}\{\text{Fe}_{\text{diss}}\} \ll \text{BP}/\text{BC}\{\text{Fe}_{\text{diss}}\}$ , is obviously counteracted during the *E* process. Indeed, for the *C* crystal, densities of all recombination centers increase with the  $\text{CR} \rightarrow \text{CE}$  step (see Fig. 4). Unfortunately, it was not possible to measure reliably  $\tau_{\text{Eff}}$  and  $\{\text{Fe}_{\text{diss}}\}$  after the *E* step for the *A* crystal.<sup>16</sup> However,  $\text{AE}/\text{AR}\{NJV\} > \text{CE}/\text{CR}\{NJV\} > 1$  (see Fig. 5) suggests a flow of dissolved iron atoms during stage *E* into the NJV, due to the high firing temperature (800 °C) and additional partial dissolution of iron-containing precipitates in the bulk. For the *B* crystal  $\text{BE}/\text{BR}\{NJV\} < 1$ , which supports the suggestion of a total dissolution of existing iron-containing precipitates already during the *P* stage.<sup>12</sup>

## D. Discussion

The results presented above were already commented with possible explanations of the observed effects. In the following, we will try to build a consistent picture of the iron-related processes, where the described observations will be included. It should be stressed however that our picture will lack information about impurities different from iron.

The formation mechanism of the NJV traps, already described in Ref. 12, will be briefly repeated. High temperatures during the *P*-diffusion process initiate a partial dissolution of the iron precipitates in the bulk of the samples. Due to the gettering of iron in the *P*-diffused layer, a flow of iron

atoms exists from the bulk to the highly doped *n*-layer. On the other hand, the *P*-diffusion process involves injection of various defects and complexes into the NJV.<sup>24</sup> Fast cooling after the diffusion process causes the interaction of Fe atoms with these injected species and the formation of the NJV traps. At the same time, iron atoms, dissolved from the precipitates in the bulk, re-precipitate upon cooling after *P*-diffusion. The effectivity of the re-precipitation is strongly enhanced by remaining precipitates, which serve as sinks for the Fe atoms. During the *R* stage, re-precipitation continues, however Fe atoms from the dissolving NJV traps are now entering the bulk, partially compensating the loss of dissolved Fe. Obviously, the presence of the  $\text{Si}_3\text{N}_4$  layer enhances passivation/dissolution of the NJV defects. This effect of silicon nitride was previously reported<sup>25</sup> and attributed to the passivation of Fe related defects by hydrogen, which was emitted from the  $\text{Si}_3\text{N}_4\text{:H}$  layer at processing temperatures. The following *E* stage mirrors the *P*-diffusion stage, causing again a partial dissolution of precipitated Fe, which increases the formation of NJV traps, but leads also to an increase in the dissolved iron fraction in the bulk. However, due to the short time of heating and the lower processing temperature, the effect of the *E* stage is much milder in comparison to the *P* stage.

Several ways for tailoring the solar cell fabrication process to achieve low defect activity despite large total iron content can be proposed from our results. Obviously, for a complete gettering of iron during the *P*-diffusion stage, the process parameters should be accommodated to  $\{\text{Fe}_{\text{tot}}\}$  in the crystal. For example, for the *B* crystal, all precipitates dissolve during *P*-diffusion. Therefore, the standard process used in the present work will safely withstand the specified amount of iron contamination.<sup>12</sup> The strategy for the whole fabrication process in the case of larger Fe content could involve the following approaches proposed in Ref. 15: extension of the *P*-diffusion time, slow cooling rate after the diffusion, and/or additional annealing sequences at moderate temperatures.

If significant changes to the parameters of the *P*-diffusion stage are not acceptable, one could change the sequence of detailed processing steps. Namely, the annealing related to the *R*-stage could be performed at the very final stage of processing. This would reduce significantly the effect of the precipitate dissolution during the *E*-stage.

## IV. SUMMARY

Formation and behavior of defects during the solar-cell fabrication from iron contaminated Si crystals were analyzed. Three groups of the defects could be specified. The first group is formed as a result of the phosphorous-diffusion process. The defects are located in NJV of the  $n^+p$ -junction and determine the value of dark saturation current of the cells. Their density is proportional to the total iron concentration  $\{\text{Fe}_{\text{tot}}\}$  in the as-grown crystal. The second group consists of iron atoms which are dissolved in the bulk of the solar cell. The portion of the dissolved iron  $\{\text{Fe}_{\text{diss}}\}$  is not directly proportional to  $\{\text{Fe}_{\text{tot}}\}$ , but depends on the thermal history of the crystal. Iron precipitates in the bulk serve both

as sources and as sinks for the dissolved iron atoms depending on the process temperature. The NJV traps will also supply dissolved iron atoms upon thermal treatments. The last group contains iron-silicide precipitates, which together with other, non-iron-related defects and dissolved iron atoms determine the bulk carrier lifetime of the crystal.

From our results, it is obvious that routinely performed estimations of the dissolved iron concentration  $\{\text{Fe}_{\text{diss}}\}$  in the wafers using lifetime measurements are not enough for correct optimizing of the solar cell fabrication processes. Instead the knowledge of the total iron concentration  $\{\text{Fe}_{\text{tot}}\}$  in the crystals is absolutely necessary. Fortunately, the proposed HTAQ sequence allows a reliable determination of  $\{\text{Fe}_{\text{tot}}\}$ . It was confirmed that the standard solar cell fabrication process<sup>16,18</sup> withstands iron contamination at a level of  $\{\text{Fe}_{\text{tot}}\} \approx 3 \times 10^{12} \text{ cm}^{-3}$ . Modification of the solar cell fabrication process for higher values of  $\{\text{Fe}_{\text{tot}}\}$  may include changes to the processing parameters of the phosphorus diffusion stage as well as changes in the sequence of the processing steps.

## ACKNOWLEDGMENTS

The authors would like to thank the colleagues from Bosch Solar Energy AG for growing the crystals and the preparation of wafers.

The work was supported by the German Ministry for Education and Research under contract 03SF0398K (xμ-Material) in the framework of the Excellence Cluster Solar Valley Central Germany.

<sup>1</sup>J. Hofstetter, J. F. Lelièvre, C. del Canizo, and A. Luque, *Mater. Sci. Eng. B* **159–160**, 299 (2009).

<sup>2</sup>G. Coletti, R. Kvannd, V. D. Mihailitchi, L. J. Geerligs, L. Arnberg, and E. J. Øvrelid, *J. Appl. Phys.* **104**, 104913 (2008).

<sup>3</sup>R. Kvannd, L. J. Geerligs, G. Coletti, L. Arnberg, M. Di Sabatino, E. J. Øvrelid, and C. C. Swanson, *J. Appl. Phys.* **104**, 064905 (2008).

<sup>4</sup>I. E. Reis, S. Riepe, W. Koch, J. Bauer, S. Beljakowa, O. Breitenstein, H. Habenicht, D. Kreßner-Kiel, G. Pensl, J. Schön, and W. Seifert, in *Proceedings of the 24th European Photovoltaic Solar Energy Conference*, edited by W. Sinke, H. Ossenbrink, and P. Helm (Hamburg, Germany, 2009), pp. 2144–2148.

<sup>5</sup>A. A. Istratov, H. Hieslmair, and E. R. Weber, *Appl. Phys. A* **69**, 13 (1999).

<sup>6</sup>T. Mchedlidze and J. Weber, *Phys. Status Solidi RRL* **8**, 228 (2014).

<sup>7</sup>K. Sumino, *J. Physique* **44**, C4-195 (1983).

<sup>8</sup>K. Lauer, M. Herms, A. Grochocki, and J. Bollmann, *Solid State Phenom.* **178–179**, 211 (2011).

<sup>9</sup>B. Shen, X. Y. Zhang, K. Yang, P. Chen, R. Zhang, Y. Shi, Y. D. Zheng, T. Sekiguchi, and K. Sumino, *Appl. Phys. Lett.* **70**, 1876 (1997).

<sup>10</sup>J. Jablonski, B. Shen, T. R. Mchedlidze, M. Imai, and K. Sumino, *Mater. Sci. Forum* **196–201**, 1859 (1995).

<sup>11</sup>D. Abdelbarey, V. Kveder, W. Schröter, and M. Seibt, *J. Appl. Phys.* **108**, 043519 (2010).

<sup>12</sup>T. Mchedlidze and J. Weber, *Phys. Status Solidi B* **251**, 1608 (2014).

<sup>13</sup>V. Vähänissi, A. Haarahiltunen, M. Yli-Koski, and H. Savin, *IEEE J. Photovoltaics* **4**, 142 (2014).

<sup>14</sup>S. Dubois, O. Palais, M. Pasquinelli, S. Martinuzzi, C. Jaussaud, and N. Rondel, *J. Appl. Phys.* **100**, 024510 (2006).

<sup>15</sup>V. Vähänissi, A. Haarahiltunen, H. Talvitie, M. Yli-Koski, and H. Savin, *Prog. Photovolt. Res. Appl.* **21**, 1127 (2013).

<sup>16</sup>K. Lauer, C. Möller, K. Neckermann, M. Blech, M. Herms, T. Mchedlidze, J. Weber, and S. Meyer, *Energy Proc.* **38**, 589 (2013).

<sup>17</sup>T. Mchedlidze, L. Scheffler, J. Weber, M. Herms, J. Neusel, V. Osinniy, C. Möller, and K. Lauer, *Appl. Phys. Lett.* **103**, 013901 (2013).

<sup>18</sup>J. Szlufcik, F. Duerinckx, E. van Kerschaver, R. Einhaus, A. Ziebakowski, E. Vazsonyi, K. D. Clercq, J. Horzel, L. Frisson, J. Nijs, and R. Mertens, in *Proceedings of the 14th European Photovoltaic Solar Energy Conference*, edited by H. A. Ossenbrink, P. Helm, and H. Ehmann (WIP-Munich, Germany, 1997), p. 380.

<sup>19</sup>J. L. Gray, in *Handbook of Photovoltaic Science and Engineering*, edited by A. Luque and S. Hegedus (John Wiley & Sons, Ltd, West Sussex, England, 2003), p. 92.

<sup>20</sup>K. Bouzidi, M. Chegaar, and M. Aillerie, *Energy Proc.* **18**, 1601 (2012).

<sup>21</sup>J. H. Werner, *Appl. Phys. A* **47**, 291 (1988).

<sup>22</sup>V. Mikhelashvili, G. Eisenstein, V. Garber, S. Fainleib, G. Bahir, D. Ritter, M. Orenstein, and A. Peer, *J. Appl. Phys.* **85**, 6873 (1999).

<sup>23</sup>J. Hofstetter, D. P. Fenning, J.-F. Lelievre, C. del Cañizo, and T. Buonassisi, *Phys. Status Solidi A* **209**, 1861 (2012).

<sup>24</sup>A. Bentzen, A. Holt, J. S. Christensen, and B. G. Svensson, *J. Appl. Phys.* **99**, 064502 (2006).

<sup>25</sup>P. Karzel, A. Frey, S. Fritz, and G. Hahn, *J. Appl. Phys.* **113**, 114903 (2013).